2014 Vol. 41, No. 9 / September 2024 / Journal of the Optical Society of America B Research Article

Journal of the Optical Society of America B

OPTICAL PHYSICS

Multi-objective scintillator shape optimization for increased photodetector light collection

G. Reales,[1,2,*] F. van Keulen,[1] A. M. Aragón,[1] J. F. L. Goosen,[1] and A. Bornheim[2]

[1]Faculty of Mechanical Engineering, Delft University of Technology, Mekelweg 2, 2628 CD, Delft, The Netherlands
[2]California Institute of Technology, Pasadena, California 91125, USA
*g.realesgutierrez@tudelft.nl

Received 14 May 2024; revised 14 July 2024; accepted 15 July 2024; posted 17 July 2024; published 14 August 2024

Inorganic scintillators often use exotic, expensive materials to increase their light yield. Although material chemistry is a valid way to increase the light collection, these methods are expensive and limited to the material properties. As such, alternative methods such as the use of specific reflective coatings and crystal optical shapes are critical for the scintillator crystal design procedure. In this paper, we explore the modeling of a scintillator and silicon-photomultiplier (SiPM) assembly detector using GEANT4. GEANT4, an open-source software for particle–matter interaction based on ray-tracing, allows the modeling of a scintillator-based detector while offering methods to simplify and study the computational requirements for a precise calculation of the light collection. These studies incorporate two different geometries compatible with the barrel timing layer (BTL) particle detector that is being built for the compact muon solenoid (CME) experiment at CERN. Furthermore, the geometry of our model is parameterized using splines for smoother results and meshed using GMSH to perform genetic numerical optimization of the crystal shape through genetic algorithms, in particular non-dominated sorting genetic algorithm II (NGSAII). Using NSGA-II, we provide a series of optimized scintillator geometries and study the trade-offs of multiple possible objective functions including the light output, light collection, light collection per energy deposited, and track path length. The converged Pareto results according to the hypervolume indicator are compared to the original simplified design, and a recommendation towards the use of the light collection per energy deposition and track path length is given based on the results. The results provide increases in this objective of up to 18% for a constant volume for a geometry compatible with the current design of the BTL detector.

https://doi.org/10.1364/JOSAB.529434

1. INTRODUCTION

Scintillation materials can absorb energy from ionizing radiation and convert it to visible light, making them useful for detecting and measuring radiation in a variety of applications. Scintillator crystals are commonly used in the medical sector [1], radiation safety, and high-energy physics research, among other fields [2,3]. As components of medical imaging technologies, e.g., positron emission tomography (PET) or single-photon emission-computed tomography (SPECT) [4], they are a key material for obtaining high resolution of the body's anatomy and function, allowing for early detection of diseases such as cancer or cardiovascular diseases [5]. Furthermore, in high-energy research, scintillator crystals play a key role in the study of fundamental particles and the nature of matter and energy [6]. Lastly, as radiation detectors used in the security sector, they help to monitor the use of radioactive material in airports, nuclear power plants, and other critical infrastructure [7,8].

In spite of their importance to the aforementioned industries, solid inorganic scintillation materials are often prohibitively expensive. In particular, LYSO:Ce crystals cost up to $4000/kg, constituting more than 50% of the total production cost for scintillator crystals [9]. The factors that contribute to this high cost are the rare materials used—often these crystals require scarce resources such as rare earths (e.g. cesium or thallium)—the required manufacturing methods, such as crystal pulling or vapor transport, and specialized tooling and machinery. There is a trend to mitigate these costs by searching for cheap organic and polymeric scintillator materials and new manufacturing techniques. Pla-Dalmau *et al.* [10] shows how the extrusion technique applied to plastic scintillators reduces the cost from $40/kg to the order of $7/kg compared to other techniques.

Even if the future of organic scintillators is promising, plastic materials do not comply with the radiation hardness, high density, and light yield (L_Y)—photons created per energy deposited by ionizing sources—required for their use in high-energy physics experiments, leading to the use of expensive inorganic

scintillation crystals [11–13]. The need for inorganic crystals makes their design critical, including their optical coupling materials, assembly to the photodetector, and a crystal geometry to increase the light collection with the lowest amount of material possible, all of which is directly proportional to the crystal cost. The usual high refractive index of scintillators, such as CsI(Tl) or BaF_2, including their surface finish or reflective coatings, can help reflect and redirect light towards the attached photodetector, increasing the overall light collection and the signal-to-noise ratio of the detected signal [14]. However, experimentally testing the light collection of multiple shapes is time-consuming and expensive.

The complexity of the scintillation crystal design and optimization can be seen in the literature, with various optimization examples that include their chemical and design criteria. We can find examples of chemical optimization in Khodyuk *et al.* [15], which provides a combinatorial algorithm to predict the light yield of the crystals depending on the composition of the material. In Berg *et al.* [16], we can find an example of the effect of the surface finish of the crystals on their light collection. This study shows, through simulation and experimentation, that samples with rougher surfaces can improve light collection. The shape of different crystals can also affect the efficiency of the system. Danevich *et al.* [17] experimentally show that a hexagonal crystal improves the energy resolution compared to a cylindrical shape. Knowing that the shape of these crystals affects their timing and light collection, Min *et al.* [18] perform a parameter study of the thicknesses of the crystals and obtain good correlation with the experimental results. Li *et al.* [19] introduce a first-sizing optimization using genetic algorithms for the optimization of three design parameters through the Monte Carlo N-Particle software (MCNP, [20]). Direct experimental testing on multiple shapes of inorganic scintillation crystals without any reflective coatings is tested in Xie *et al.* [14]. The results of the experiments showed a higher precision for the tetrahedral shapes compared to those of the other geometries studied. Zhao *et al.* [21] studied the coupling shape between SiPM (silicon-photomultiplier) and scintillator, where a runway-shaped groove in the contact region could improve the non-uniformity with low light output loss. Although the literature already cited uses numerical models to explain and enhance the light collection of the scintillator crystals, much of the research is focused on costly and time-consuming experimental results.

The use of numerical modeling and optimization can reduce experimental time and cost. However, the procedure to perform these modelings and optimizations is not evident. Particle–matter interaction software is based on ray-tracing and Monte Carlo, such as GEANT4 [22], dealing with results in the form of stochastic data. This leads to difficulties in the available numerical optimization techniques, with the need for gradient-free optimization [23] techniques to numerically model multiple shapes of scintillation crystals and optimize them for improved light collection measurements. These optimization techniques avoid the need for analytical expressions for the objective derivatives concerning the design variables. In particular, the viability of these algorithms for multi-objective optimization can help to identify trade-offs between conflicting objectives with a global design space exploration.

Parameterization and optimization of scintillation crystal surfaces can further enhance their efficiency compared to parametric or size optimization. Shape optimization can reduce the light reabsorption within the crystals and take into account the effect of localized higher-energy depositions with regard to the photodetector interface location. While these materials are not easy to machine, through advances in free-form optical manufacturing [24] and numerical optimization techniques, we should reconsider the way scintillation crystals are designed nowadays. Furthermore, the lack of numerical optimization examples in the literature and the stochastic nature of the problem do not provide a clear design objective for numerical optimization algorithms and methods to calculate them in an efficient manner.

In this paper, we propose a simulation model for a scintillation-based particle detector and evaluate its sensitivity to manufacturing tolerances. We used the state-of-the-art minimum ionizing particle detector-barrel timing layer (MTD-BTL) detector [25] to be installed at CMS-CERN as a configuration reference for our model. Starting from MTD-BTL, we propose simplification approaches and techniques for faster computational time using GEANT4, which is required for a feasible numerical optimization due to the large computational time of Monte Carlo studies. This paper further proposes a one-dimensional design space to prove the dependence of the detector light collection on the scintillator shapes and compare optimization formulations. Finally, two base geometries considered for MTD-BTL are parameterized to perform shape optimization on the scintillation crystals. The optimization is performed using the non-dominated sorting genetic algorithm II (NSGA-II, [26]) with photon count and volume objectives to understand the trade-off between the contrasting objectives. The algorithm's convergence is studied through the hypervolume of successive generations of the genetic algorithm, and the configurations with the same volume as the initial designs are post-processed to verify the optimization outputs and provide further understanding of the optimization procedure for future scintillation crystal design.

2. METHODOLOGY

Scintillator crystal modeling requires the use of specialized particle–matter interaction software. One such software is GEANT4 ([27]), an open-source Monte Carlo ray-tracing library implemented in C++, which has been extensively tested in various fields such as medical engineering and research in high-energy physics and radiation protection.

This section starts by describing the definition of the detector geometries studied in this paper within GEANT4, continues with the particle event definition for the detector characterization, and finishes with the parameterization and definition of the optimization algorithm to perform shape optimization on scintillating crystals. Although this section provides the information needed to model the scintillation phenomena, all relevant material properties used in this paper are summarized in Appendix A for clarity purposes.

A. Geometry

The detector geometry studied in this paper is based on the Barrel Timing Layer (BTL) detector [25], specifically designed for the detection of minimum ionizing particles within the Compact Muon Solenoid (CMS) detector at CERN. The BTL current configuration consists of 16 rectangular LYSO:Ce bars with 32 SiPM channels optically glued to both ends of each bar. Figure 1 shows the dimensions and tolerances used in the model, closely based on the BTL detector. The drawing represents the LYSO bars with a length of 57 mm with ±0.1 mm for the coating thicknesses. In Fig. 1, we can also see a cut section with the different layers in the optical connection consisting of an adhesive layer and protective resin layer before the SiPM, supported in an FR4 package. This bar scintillator configuration covers a continuous cylindrical area of radius 1991 mm. This configuration is designed so that it can be stacked and reduce the dead area, designed as the area where the scintillators cannot provide any sensing capabilities. However, the mechanical components and optical interfaces account for the 9.5% dead area relative to the total cylindrical area of the detector. For any further improvements and changes in the detector, we need to consider the stackability of the scintillator crystals to ensure that this dead area does not increase.

To maintain this dead area as small as possible, another configuration of interest for the detector is a geometry in which the photodetectors or SiPMs are found in the bottom flat surface of the scintillator. This tile-based configuration can reduce the dead area associated with the SiPM package, maintaining the advantages of the previously described bar configuration. In this geometry, we impose the location of the 2 SiPMs for a single tile along one of its symmetry axes, maintaining the same number of SiPMs and their characteristics to compare to the bar configuration. The sensitive area of each tile must also be comparable to the sensitive area of each scintillator bar in the previous configuration to avoid increasing the total number of channels in the detector. Figure 2 shows a lateral view and a cut section for the scintillators in the tile configuration with the respective locations of the SiPM.

As the smallest unit of the detector, we focus on these crystal modules for our setup within GEANT4, considering impacts only in a single-crystal sensitive area. The crystal geometry is constructed using a tetrahedral volumetric mesh generated with GMSH [28], and subsequently imported into GEANT4 through the points of each tetrahedral element. Notice that

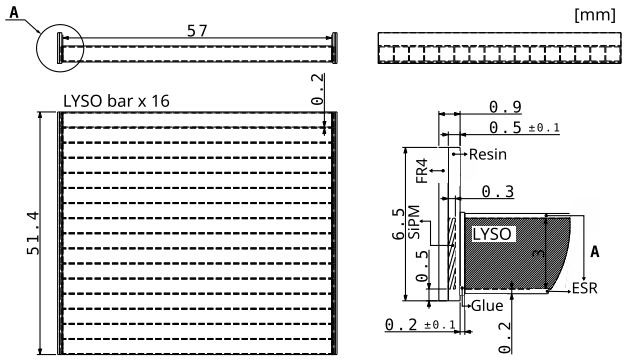

Fig. 1. Standard LYSO module schematics for BTL with tolerances used in the GEANT4 model and dimensions in mm.

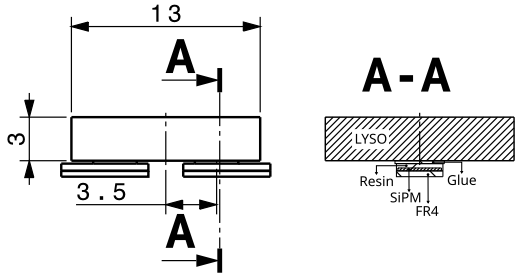

Fig. 2. LYSO-SiPM package schematics for BTL tile configuration with dimensions in mm; lateral and cut view.

while geometries defined through triangular elements that can be stored in STL format have the advantage of faster loading times in GEANT4, volumetric meshes defined through multiple volumes in the form of tetrahedral elements exhibit computational benefits, particularly when dealing with a large number of events or particle impacts. The resulting lower computational cost of volumetric meshes arises from the reduced cost to determine collision points with the next surface in the model, given a connectivity matrix for the volumetric elements. This is thoroughly tested in Poole *et al.* [29] for complex geometries.

B. Event Definition

To start a particle–matter interaction simulation within GEANT4, we need to define the event interaction that we are going to study. This simulation setup involves defining high-energy particles in a trajectory that impacts our material of interest. For this reason, we differentiate two different particle impacts of interest. To facilitate direct comparisons with experimental results in the laboratory, we model the particles as 0.511 keV gamma rays emitted from a ^{22}Na source. By simulating these specific gamma rays, which are commonly used for the characterization of BTL crystals in laboratory settings [30], we ensure that our simulation closely aligns with experimental measurements. In addition to ^{22}Na gamma rays, we also provide the option of setting the ionizing particle as muons with an energy of 2 MeV in our simulations. The use of muons aims to emulate a closer operational condition to CMS. Unlike 0.511 keV gamma rays, which are locally absorbed within the crystal, higher energies of muons enable them to penetrate the crystal and produce a trace of photons as they cross the scintillator.

The location of the particles' impact also impacts the light collection, and for this reason, two testing scenarios for particle impact positions are implemented. To create a realistic testing scenario that captures the effects of the randomized impact location under radiation sources, we apply a random distribution of the particle impact positions along the x and z coordinates within the crystal's longitudinal-sectional area. This allows us to explore how the particle trajectories influence the generation and propagation of photons within the crystal. To simplify the definition, we consider that the particles fly parallel to the y axis, perpendicular to the crystal x-z plane, which ensures the impact and a full exploration of the entire volume of the crystal with enough impacts. We further incorporate the option to run a uniform pattern impact distribution using symmetry conditions on the assembly, which allows us to simulate a representative subset

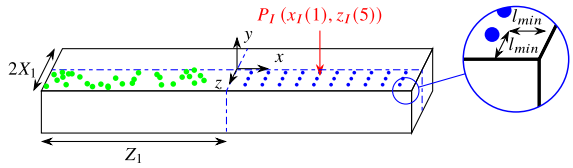

Fig. 3. Schematics of a random and uniform pattern of impacts on a crystal represented as green or blue dots, respectively, within one quarter of the crystal due to symmetry conditions. The particle is represented by a red arrow showing its perpendicular direction against the top surface of the initial design of the crystals. The symmetry conditions of the crystal are represented as blue dash-dotted lines.

of impact positions efficiently. Uniform impact distribution locations can reduce the number of simulations required to comprehensively evaluate the scintillator response to particle interactions.

This uniform distribution can be defined with a number of impacts along the axes x and z, n_x and n_z, with a total number of impacts equal to $n_I = n_x n_z$. The impacts are located along the z and x axes with a minimum distance to the edges of the crystal, $l_{\min}$, resulting in a constant distance spacing along each axis. We can write the location of each impact point as

$$x_I(i) = X_1 - l_{\min} - \frac{X_1}{n_x}(i-1), \quad i \in \{1, \ldots, n_x\},$$

$$z_I(j) = Z_1 - l_{\min} - \frac{Z_1}{n_z}(j-1), \quad j \in \{1, \ldots, n_z\},$$

$$P_I(i, j) = (x_I(i), z_I(j)), \tag{1}$$

where z_i and x_i are each impact point numbered from 1 to the number of points and each axis. P_I is a matrix of size $n_x \times n_z$ that contains all impact sites. In these equations, Z_1 and X_1 represent the half-length of the crystal for the axes x and z, respectively.

Figure 3 shows a schematic of the Monte Carlo impacts in the bottom left top quarter of the crystal and an example of the uniform impact distribution for $n_x = 10$ and $n_z = 5$ on the bottom right quarter. Given the symmetry conditions, only one-quarter of the surface needs to be covered by the events. Figure 3 also shows the system of reference for the impact definition, the characteristic half-lengths of the geometry Z_1 and X_1, and the minimum lengths respected to the edges of the geometry as $l_{\min}$.

C. Scintillation

For the model under investigation, we have chosen LYSO:Ce as the scintillator material, with reference to the BTL detector. The selection of LYSO:Ce is motivated by its widespread use in the industry, its proven radiation hardness, high density, and light yield (L_Y) [25].

To model the scintillation phenomena, we need to calculate the number of photons created within the scintillator (N_γ) in each time step of our ray-tracing algorithm. A Gaussian distribution is used to model this number of photons as

$$\mu_{N_\gamma} = E \cdot L_Y, \tag{2}$$

$$\sigma_{N_\gamma} = r_s \cdot \sqrt{E \cdot L_Y}, \tag{3}$$

$$N_\gamma = N(\mu_{N_\gamma}, \sigma_{N_\gamma}). \tag{4}$$

In these equations, E represents the energy deposited by an ionizing particle within the crystal during each time step and r_s represents the resolution scale or possible deviation of the location of the mean value of the distribution. The normal distribution from which we extract N_Y is determined by its standard deviation σ_{N_γ} and mean μ_{N_γ} based on the previously defined L_Y, r_s, and E.

While r_s and L_Y are parameters measured experimentally, the mean energy deposited per track length of the impacting particle, $\frac{\partial E}{\partial x}$, is precomputed for the different materials, particles, and incident energies and stored in table data [27]. During runtime, the values $\frac{\partial E}{\partial x}$ are recovered, interpolated, and used to define the time step size according to an energy loss limit. This energy deposition exhibits stochastic behavior, following a Landau distribution. The Landau distribution notably leads to tails at large energy-deposition values caused by possible knock-on electrons turning themselves into ionizing particles, influencing the outcome of the photons detected.

Once the number of photons created is calculated, we need to define their time characteristics. This behavior can be described by an exponential rise and decay process, i.e.,

$$N_\Gamma(t) = \frac{N_\gamma}{\tau_d - \tau_r}\left(e^{-\frac{t}{\tau_d}} - e^{-\frac{t}{\tau_r}}\right), \tag{5}$$

where t denotes time, and τ_d and τ_r represent the decay and rise times of the exponential growth and decay of the scintillation process, respectively [31].

The generated photons must also have a given wavelength. This wavelength is calculated through an intensity distribution function from experimental data defined as the spectrum of the scintillator. For our particular LYSO:Ce, the spectrum and L_Y are measured by Addesa *et al.* [32] and Campana and Paramatti [33]. These photons propagate through the scintillator, refract, and reflect on the optical surfaces of the detector until they are reabsorbed by the scintillator or arrive at the photodetectors. For the implementation of the scintillation constants and their intensity function within this paper, refer to Appendix A.3.

Although the high refractive index of LYSO:Ce compared to air mitigates the loss of photons to the environment, any escaping photons can create false signals in neighboring photodetectors. For this reason, it is common practice to coat or cover scintillators with a reflective layer. In our model, we employ an enhanced specular reflector (ESR) that is superposed on the crystal with an air gap to the LYSO:Ce capitalizing on the substantial refractive index difference between the air–LYSO interface [34], see Appendix A.2.D. The internal reflections then account for an optical polished surface for the LYSO–air interface, based on the surface roughness specifications for BTL of $R_a < 15$ nm and a specular reflector for the ESR.

D. Photon Detection

The photons are detected by the SiPMs, which exhibit a photon-detection efficiency (PDE) or probability of detection of the incident photons. These SiPMs are modeled as a silicon block whose PDE depends on the overvoltage (ov), or the voltage across the terminals of the SiPM above its breakdown voltage,

and the incident wavelength, λ, given by the expression

$$\mathrm{PDE}(V_{ov}, \lambda) = 0.393\left(1 - e^{-0.583 V_{ov}}\right) \cdot F_{\lambda}(\lambda). \quad (6)$$

Although V_{ov} can be modified during operation, we consider a V_{ov} of 3.5 V for comparison purposes in the subsequent simulations. This specific value is utilized in conjunction with the PDE data obtained from the manufacturer's datasheet to scale the function F_{λ}, see Appendix A.4. This PDE is implemented such that when a photon impacts the SiPM we retrieve a value from a uniform distribution, $U(0, 1)$, and the photon is considered detected if this value is higher than its corresponding PDE. The total number of photons detected, or light collection (L_C), can be calculated from each impact and the summation

$$L_C^i = \begin{cases} L_C^{i-1} + 1 & \text{if } u_i \sim U(0,1) > \mathrm{PDE}(V_{ov}, \lambda_i) \\ L_C^{i-1} & \text{if } u_i \sim U(0,1) \leq \mathrm{PDE}(V_{ov}, \lambda_i) \end{cases}, \quad (7)$$

where u_i denotes a value taken from a uniform random distribution, and λ_i represents the wavelength of the impacting photon i. Whether detected or not, all photons that reach the SiPM are subsequently terminated in the next calculation step within GEANT4. This photon-killing procedure simulates their absorption within the SiPM and reduces the computational cost of these traces.

E. Numerical Optimization

Due to the inherently statistical nature of the results obtained from GEANT4, calculating the sensitivities for this problem presents a challenge. As a solution, we turn to the use of genetic algorithms inspired by natural selection, which have demonstrated their effectiveness as heuristic approaches to solving complex problems without the need for exact analytical solutions. In particular, we have chosen to use the non-dominated sorting genetic algorithm II (NSGA-II, [26]). NSGA-II uses an initial random population of solutions that evolves in successive generations into candidate optimal solutions through crossover, mutation, selection, and non-dominant sorting of each population.

Several indicators assess the quality of populations in multiobjective optimization. Li and Yao [35] survey various quality indicators, organizing them by the specific aspect of optimization quality they measure. We use the hypervolume indicator [36] which focuses on the convergence of the optimization and the spread of the solution. This measure is commonly used due to its robustness and practical implementation compared to other indicators. This hypervolume measure can be defined as

$$\mathrm{HV}(Q, P_r) = \kappa\left(\bigcup_{q \in Q} \prod_{i=1}^{n_o} [q[i], P_r]\right), \quad (8)$$

where κ denotes the Lebesgue measure, Q and q represent a population and each one of its individuals, and n_o is the total number of objective values of each individual. For the calculation of this hypervolume, we need to define a reference point. The selection of this point must be chosen as the nadir point—defined as the worst possible value for all objectives—or the closest approximation to it. In our case, we know the ranges of the volume given the range of the design variables, and the light collection, energy deposition, and length paths within the crystal are always greater than or equal to zero. Taking this into account, we define the reference point

$$P_r = (H, V) = (0, 4 Z_0 Y_0 l_{\max}). \quad (9)$$

The hypervolume indicator can be understood as a measure of the area of the Pareto front with respect to this reference point, P_r. Although the hypervolume has limitations due to an increase in the runtime of $O(n_o)$ with each optimization dimension, its sensitivity to any modification in the Pareto front and the fact that it also provides information on the spread of the set make it one of the most common convergence indicators for multiobjective optimizations [37].

Although the hypervolume provides a measure of the change in the ranked population provided by NSGA-II, the randomness inherent in the algorithm does not guarantee that an absence of change in two consecutive generations is indicative of having discovered an optimal design. For this reason, we utilize the delay parameter n_h, comparing the hypervolume of the last generation to that of n_h generations prior. For our convergence criterion, we use this delayed hypervolume normalized to the initial generation hypervolume, which must be lower than a given tolerance *Tol*. The convergence criteria and the NSGA-II algorithm are represented in Fig. 4.

Once we have defined the optimization algorithm, we need to provide the design variables and objective functions of the problem. To be able to perform shape optimization on the crystals, we parameterize the shape of the crystal along the y-z cross section using a series of control points and Catmull–Rom splines. To simplify the definition of control points, we use symmetry conditions along the x-y plane and uniformly distribute control points along the z axis. Figure 5(a) exemplifies this parameterization of the bar configuration with the original flat design superposed by an optimized design, its splines, and control points. Additionally, we provide one last degree of freedom: the crystals' length or width. To maintain a constant sensitive area in the detector, this degree of freedom is constrained by

$$Z_1 X_1 = Z_0 X_0, \quad (10)$$

where Z_1 and X_1 represent the half-width and half-length, and Z_0 and X_0 are the half-width and half-length of the original configuration. This constraint avoids increasing the number of photodetector channels to cover the same sensitive area as the original detector. The top view of the parameterized crystal shown in Fig. 5(b) exemplifies these width and length changes. The SiPM is always maintained at the X_1 location.

Although the splines fully represent the geometry, the mesh must capture its curvature. We recommend a minimum of twice the number of mesh nodes along the splines compared to the number of control points, which should be higher than our number of impacts through the z axis, n_z.

In numerical optimization algorithms, the results are affected by the parameterization of the problem. For this reason, if we want to study a second configuration, we either need to make sure it is attainable with our current parameterization scheme or provide a different one. To study the tile configuration, with

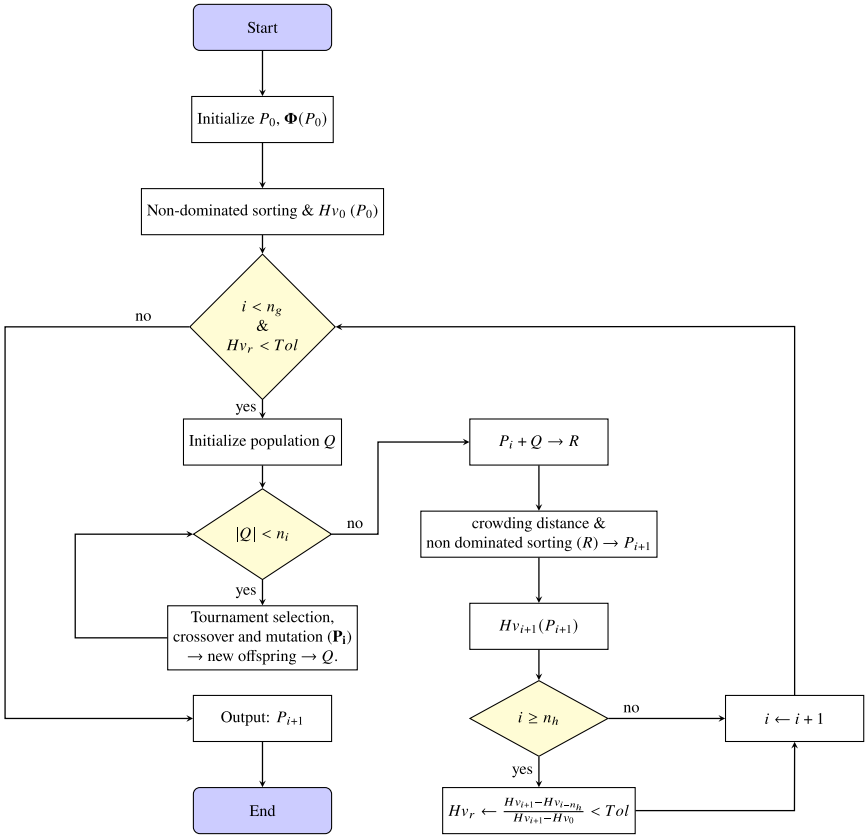

Fig. 4. NSGA-II formulation flowchart.

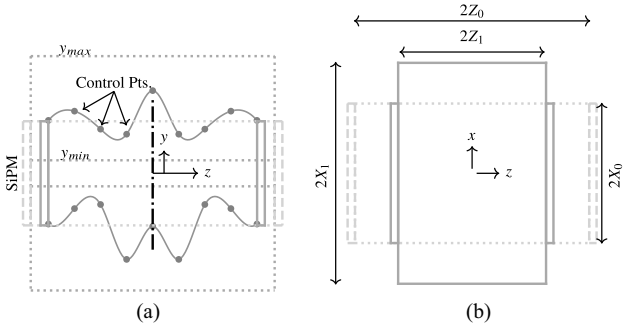

Fig. 5. Lateral and top view of the parameterized bar-shaped crystal. (a) shows the x-y plane with control points along z defining the top and bottom surfaces with their maximum and minimum. (b) shows the z-x view with changes in width and length according to the constant sensitive area constraint.

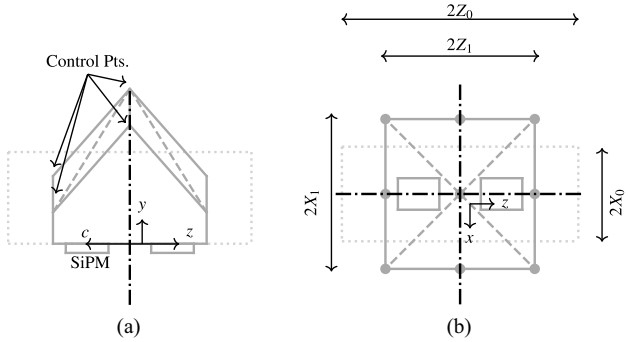

Fig. 6. Lateral and bottom view of the parameterized tile-shaped crystal with two nodes per x section. (a) shows the x-y plane with control in each vertex. (b) shows the z-x view with changes in width and length according to the constant sensitive area constraint.

the SiPMs in the bottom x-z plane, see Fig. 2, we parameterize the top x-z plane through nodes along two lines in the z direction at locations $x = \{0, X_0\}$. We exemplify this assembly and parameterization in Fig. 6. The parameterization of this new configuration uses two planes of symmetry along $z == 0$ and $x == 0$. This design is no longer possible to extrude, and the bottom surface has a new variable in terms of the location of the SiPMs, the center of which is imposed in a location z along the line $x = y = 0$. As we still need to maintain a constant sensitive area for comparison with the original geometry, we define the center location of the SiPMs with respect to each configuration value Z_1 as

$$c = Z_0 Z_S,\ Z_S \in [0,\ 1]. \tag{11}$$

Equation (11) defines the location of the SiPM in z, c, with a new design variable Z_S constrained between a value of 0 and 1.

The optimization formulation for the bar configuration can then be written as

$$[\Phi,\ Z_1,\ Z_s] = \underset{\Phi, V}{\arg\min} \quad \Phi(\boldsymbol{\theta},\ Z_1,\ Z_s) \& V(\boldsymbol{\theta},\ Z_1), \tag{12a}$$

$$\text{subject to}: \quad X_1 Z_1 = Y_0 Z_0, \tag{12b}$$

$$Z_o \in [Z_{\min}, Z_{\max}], \tag{12c}$$

$$\boldsymbol{\theta} \in [y_{\min}, y_{\max}], \tag{12d}$$

$$Z_s \in [zs_{\min}, zs_{\max}], \tag{12e}$$

where the list $\boldsymbol{\theta}$ contains the location along the y axis of each control point of the top and bottom splines, as depicted in Fig. 5, and Z_1 is the half-length, following symmetry conditions, of the crystal. Furthermore, the design variables $\boldsymbol{\theta}$, Z_s, and Z_1 are limited within a specific range relative to the default design values. Notice that the variable c is only used in the tile configuration to displace the SiPM locations. For the bar configuration, the SiPM position can be imposed through $zs_{\min} = zs_{\max}$ or by removing this design variable from the formulation. The objective values in Eq. (12a) consist of two functions: the total volume of the crystal V and a measure Φ obtained from the distribution of photons that impact the photodetectors. The total volume V is directly related to the crystal cost and prevents larger volumes favoring larger energy deposition through longer path lengths within the scintillator. This volume V is calculated by the sum of the volume of each tetrahedral element,

$$V = \sum_{e=1}^{N_e} \mu_e, \tag{13}$$

where μ_e represent the volume of the tetrahedron e in a mesh of N_e elements.

The measure Φ must be a measure of the distribution of detected photons. In this paper, we study three different ways to define Φ. The first approach is to use L_C, Eq. (7), or the sum of all detected photons. Another objective distribution worth studying is the light output L_O, or the photons detected per unit of energy deposited in the crystal and SiPM,

$$L_O = \frac{L_C}{E_e}, \tag{14}$$

with E_e the energy deposited in the crystal during the event, measured in MeV. Equation (14) characterizes the performance of the crystal with respect to different impact particles for a constant cross-sectional area. However, if the impacts have multiple track lengths along the crystal, which is ensured if we modify its thickness, L_O loses information pertinent to the total number of photons created or energy deposited. This loss of information means that we can have a large relative energy deposition in the SiPMs compared to the energy deposited within the crystal, while the total number of photons detected is too small to actually measure.

We define a new objective L_{SP} as the total number of photons detected per unit of energy deposited in the crystal and track path length (which we call pseudo-stopping-power), i.e.

$$L_{\text{SP}} = \frac{L_C}{S_P} = \frac{L_C l_\mu}{E_e},$$

where l_μ represents the total path length of the ionizing particle within the scintillator for the event in which we calculate L_{SP}.

In all cases, all photon count measures have a positive value, and as NSGA-II minimizes the objectives, we need to negate the objective to maximize the light measure received by the detector. Furthermore, these values are not constant per event, and we must consider their behavior as a distribution. We propose the use of the average and mean as initial values for the optimization of these distributions. The studied objectives can be condensed into

$$\Phi \in \left\{-\overline{L_C}, -\widetilde{L_C}, -\overline{L_O}, -\widetilde{L_O}, -\overline{L_{\text{SP}}}, -\widetilde{L_{\text{SP}}}\right\}, \tag{15}$$

where the straight line, $\overline{\Phi}$, implies the average of the distribution and the tilde, $\widetilde{\Phi}$, represents the median.

3. RESULTS

In this section, we present a summary of the results obtained from the GEANT4 simulations. This includes an evaluation of the default geometry for BTL, possible simplifications and their sources of error, a one-dimensional design space study to understand the effect of the crystal shape on multiple objectives, and numerical optimization results for the two proposed parameterizations in the previous section. The section ends with a verification of the results obtained in the optimization.

A. Default Geometry

Our initial focus is to characterize the GEANT4 results for the default geometry and explore the impact of different parameters on the simulation. This analysis provides valuable information on the design space, computational time, and feasibility of numerical optimization for this problem. For these simulations, we employ a Monte Carlo or random distribution to define the x and z location of the particles' impacts created, considering both ^{22}Na gamma rays with 0.511 MeV energy and muons with 2 MeV energy. By using both of these event definitions, we can assess the scintillator's performance under different scenarios.

The results depicted in Fig. 7(a) show the geometry schematic for the 16 LYSO:Ce bars accompanied by the corresponding light output L_O distributions for both types of particles, muons and gamma rays. On examination of the histograms of L_O from Fig. 7(a), it becomes apparent that muon impacts exhibit a smaller interquartile range (IQR) and smaller means, compared to ^{22}Na impacts. In both cases, the difference between the mean and the P_{50} (median) values in these distributions is below 0.2%, indicating a near-symmetric behavior. The lack of skewness comes from the optical processes occurring within GEANT4, modeled as Gaussians. The influence of the light yield, governed by a Landau distribution, has been considered through the division of energy deposition in Eq. (14). Due to the slight error between the P_{50} and the mean, we can fit these results to a sum of Gaussian distribution with accurate predictions. This provides a model simplification for the entire GEANT4 model and a comparison between the resulting Monte Carlo studies for different model parameters. The fitting function can be written as

$$N_f(x) = \sum_i^{n_f} a_i \frac{1}{\sqrt{2\pi\sigma_i^2}} \cdot e^{-\frac{(x-\mu_i)^2}{2\sigma_i^2}}, \tag{16}$$

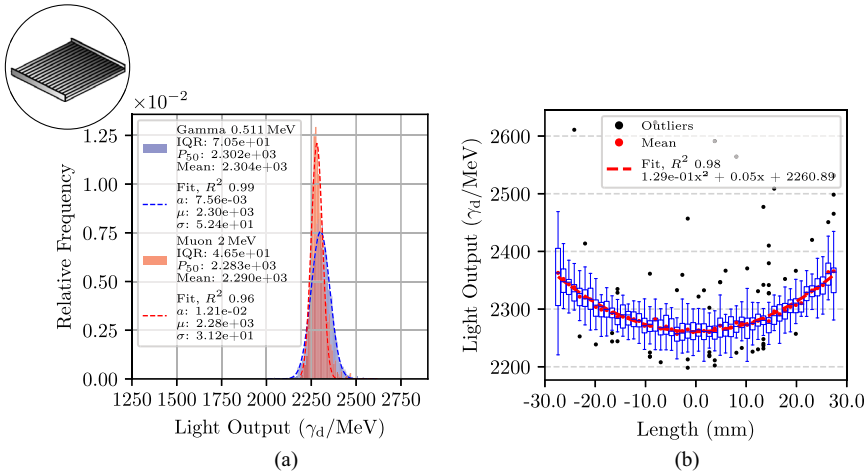

Fig. 7. Light output characteristics of the default geometry with 16 LYSO bars and 32 SiPMs. (a) shows the resulting light output distribution per SiPM for muons (μ) and gamma rays of 2 and 0.511 MeV respectively, with a fit to a linear combination of normal distributions. (b) shows a box plot of the averaged light collection between both SiPMs depending on the impact location along the length of the crystal.

with μ_i, σ_i, and the amplitude, a_i, as the fitting parameters. These parameters represent the mean, standard deviation, and amplitude of each normal distribution up to n_f. The fitting parameters are initialized to

$$\sigma_1 = i \cdot \sigma_{i>1} = \sigma(f), \quad a_i = \max(f),$$
$$\mu_1 = \mu(f), \quad \mu_{i>1} = \mu(f) + \sigma(f)/i, \tag{17}$$

where f refers to the relative frequency—the proportion of observations in a given interval of the histogram compared to the total number of observations—of the subsequent histogram. The fit is performed using a least squares algorithm with all the data from each event in GEANT4.

The statistical nature of L_O depends on the length of the photon path until detection and its probability of self-absorption within the crystal, see Appendix A.2.B. Figure 7(b) shows the distribution of L_O as a function of the location of the impact along the crystal in the z axis direction, which can be considered as a measure of the proximity of the impact to each SiPM. This figure shows that the impacts closer to the SiPM in z provide higher light collection for the same energy deposition. However, near the SiPMs, we observe a substantial increase in the L_O interquartile range. The increased IQR close to the edges of the crystal is attributed to a greater number of photon paths with substantial incidence angles to the glue interface. Despite this local deviation, the relationship between the L_O mean and its dependence on the impact of the location z can be accurately represented by fitting it to a quadratic polynomial yielding a R^2 of 0.98. This observation highlights the significance of considering the relationship between the impact and the SiPM location when analyzing the scintillator's performance and designing optimized crystal shapes.

Not only can the location of the impact affect the light collection results, but the manufacturing tolerances, see Fig. 1, can also modify the light output. To estimate the impact of manufacturing uncertainties, we perform simulations following the uniform impact description in Eq. (1) using n_x and n_z values of 4 and 15, respectively. The results of a change in the thickness of the glue layer between 0.1 and 0.3 mm are presented in Fig. 8(a), where each box corresponds to a specific thickness of the glue layer. Following the same procedure for the variation of the resin layer between 0.4 and 0.6 mm, we obtain Fig. 8(b). Both plots show a linear trend for their mean values, with a linear fit of $R^2 = 1$, maintaining a value close to the constant standard deviation within the expected geometric tolerances.

The impact of both the thickness of the glue layer and the thicknesses of the resin package on the overall light output of the device provides a similar effect; increasing the thickness of any of these elements leads to a decrease in the light output. However, the glue layer has a higher sensitivity in the final light output distribution, exhibiting a steeper slope in the linear fit. These effects can be attributed to the different refractive indexes of each material—larger for the glue layer, see Appendix A—which significantly influence photon propagation and collection.

Notice that even a slight change of 0.2 mm in any of these dimensions can result in up to an 8% variance in the nominal light output. This level of uncertainty can pose challenges when trying to measure and compare the light output of different geometries and validate the simulation results. As such, it is crucial to account for these variations when studying different scintillator geometries or assembling scintillator devices experimentally. However, these effects only lead to a translation in the objective values for comparison purposes.

B. 1D Space Study

We perform a first design space study of the effect of the shape of the scintillating crystals with a single design variable. Nonetheless, employing the same methodology as in the calculations from the previous Section 3.A, where each crystal shape was characterized using over 10,000 events for precise Monte Carlo analysis, would require excessive computational time.

To reduce computational time, we simplify the geometry, reducing the number of LYSO:Ce crystals, photodetectors, and the number of tetrahedral elements that define the geometry.

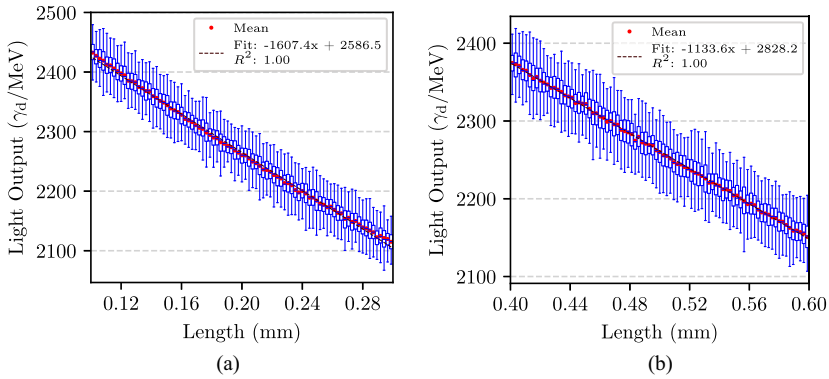

Fig. 8. Effect on the nominal distribution of the manufacturing tolerances in Fig. 1. (a) shows the L_O change for a linear change in the glue layer thicknesses around its nominal value of 0.2 mm. (b) shows the L_O change for a linear change in the SiPM resin package thicknesses around its nominal value of 0.5 mm. Both plots include a linear fit using the mean of each box plot with its formula and R^2.

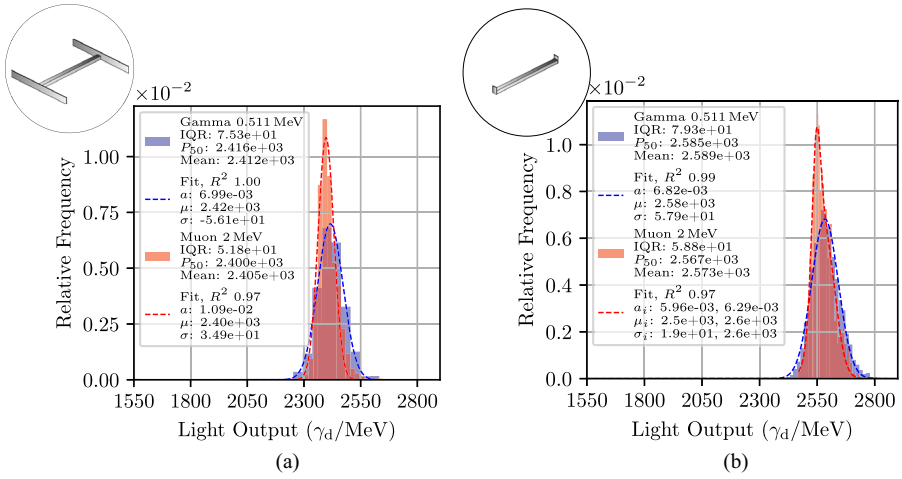

Fig. 9. Simplified LYSO:Ce module geometry L_O distributions. (a) shows the geometry and L_O distributions for a SiPM package with a full-length resin layer and a single LYSO:Ce bar. (b) shows the geometry and L_O distributions for a SiPM package with a 3 mm wide single SiPM at each end of a single LYSO:Ce bar. Both plots include results for 0.511 and 2 MeV ^{22}Na and muon impacting particles and a fit for each distribution following Eq. (17).

To investigate the impact of these simplifications on objective functions, we define and compare two configurations against the one studied in the previous section; see Fig. 7(a). In a first simplification, we remove all but one LYSO crystal and their attached SiPMs, while maintaining the original SiPM resin and FR4 package length. In a second configuration, we further reduce the SiPM package to the size of a single SiPM. These simplified geometries allow us to study the impact and sensitivity of internal reflections in the resin package to the L_O.

The results presented in Fig. 9 illustrate the L_O distributions for the two simplified geometries. The new distributions exhibit a displacement towards higher L_O values, with increases of up to 4.6% and 12% in the nominal and shortened SiPM resin packages, respectively. These improvements can be attributed to the reflections within the simplified resin geometry that would otherwise impact a nonsensitive area, improving the light collection efficiency. This effect could be reproduced through an air gap between neighboring SiPMs, increasing light collection through internal reflections while minimizing cross-talk between SiPM channels. Although there is a clear difference in the L_O distributions related to the simplified geometries, the difference between muons and the impacts of Na particles remains consistent with those observed in the default study of the geometry of the 16 LYSO:Ce bars.

From the two simplified cases, we select the nominal resin length with a single LYSO crystal as the most representative model for the optimization process. This choice balances geometric complexity and computational resources, making it a suitable compromise for the more computationally demanding optimization iterative procedure.

The next step is to parameterize the design for the optimization problem. For simplicity, we sought the most straightforward model that maintains a constant volume to allow a direct comparison with the base model. This parameterization involves using two parallelepipeds controlled by a single variable, θ, scaled between 0 and 200. This variable adjusts the thickness in the middle of the crystal while simultaneously decreasing its thickness at the edges, as illustrated in Fig. 10, maintaining a constant volume. The limiting values of θ correspond to a zero thickness in the middle or edge of the LYSO:Ce bars and a double thickness, compared to the default geometry, in the opposite location. In this geometry change,

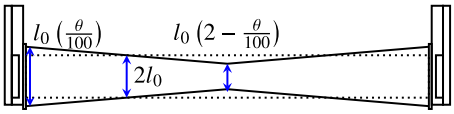

Fig. 10. Schematic for the 1D design exploration and optimization with the variable θ modifying the thickness of the crystal in the middle and edge of the crystals with the provided values in the figure, maintaining a constant volume.

the SiPM location and size remain constant, as we are only interested in the effect of the scintillator, and the resin and glue layers are changed to accommodate the size of the edge of the crystals. While these simplifications limit the design space and possible gains, they preserve the influence on the design space of the reflective surfaces and energy depositions of the ionizing particles. This study then provides information on the behavior of the objective functions concerning these parameters.

In Fig. 11, we show the mean and median for the distributions L_C, L_O, and L_{SP} obtained from the 10 runs, with the impact distributions $n_x = 4$ and $n_z = 15$, with varying values of θ between 25 and 175. The deviations observed in these distributions correspond to the variability expected in higher-dimensionality studies. In particular, L_C exhibits a larger IQR and more outliers than the other two objectives. This outcome aligns with expectations, as the Landau distributions exhibit tails that can lead to larger deviations than normal distributions for a given number of events.

Furthermore, we observe that when θ is equal to 100, these distributions show symmetric behavior—the data are balanced around its central point, and the mean, represented in blue, is equal to the median, represented in red—and we appreciate that this corresponds to the original flat configuration, refer to Fig. 7(a). However, at different values of θ, the mean and median are no longer equivalent, indicating non-symmetric behavior. This characteristic has implications for selecting the appropriate measure for each objective. For optimization L_C, the median value is more suitable, as it reduces the overall deviation in successive evaluations of the function and accounts for the influence of low values on the distribution. On the other hand, for the optimizations L_O and L_{SP}, the mean value is more conservative, being affected by the extreme or outlier values in the distributions.

In particular, we identify an optimal value θ that represents a decrease in thickness between 20% and 40% in the middle of the crystal for all objectives, resulting in a relative increase in the objective between 3 and 8%. This result is correlated with the study in Fig. 7(b) in which we observe a lower L_O sensitivity to the same energy deposition in the middle of the bar.

These results show a better fitness for the L_O and L_{SP} objectives, with minor design space roughness and stochastic errors. These results can be extrapolated to higher dimensionality spaces which maintain the same dependencies. The only factor not studied through this simplified model, included in the Eq. (12) formulation, is a volume objective to reduce material costs. This objective is expected to provide a linear design space directly proportional to the overall energy deposition in the crystals. However, the L_O objective is indifferent to the energy deposition in the system and can lead to convergence problems not studied with this simplified model.

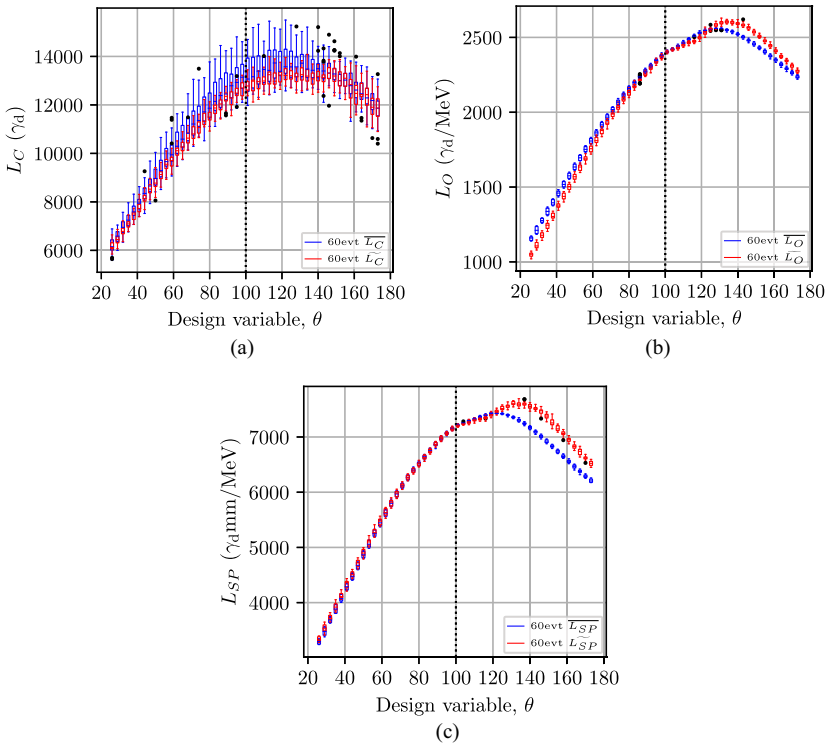

Fig. 11. Distributions for multiple objective functions according to 10 runs of 60–15 along z and 4 along x events for each θ value used. (a) shows the results for the L_C, (b) for the L_O, and (c) for the L_{SP} objective. In all cases, we use the P_{50} and average of each objective for the representation.

C. Evolutionary Optimization

A space study of low dimensionality is useful to understand the problem better and provide simple shape modifications; however, higher-dimensional design spaces allow for more freedom in designs and possibly lower minima. We use NSGA-II, following the description in Section 2.E, to get close to the Pareto fronts of the optimization problem that relates the volume and a measure of the photon collection in the photodetector.

1. Bar Configuration

We start by performing the optimization based on the bar configuration shown in Fig. 5. Given the definition of NSGA-II in Fig. 4 and the optimization definition in Eq. (12) without the design variable Z_s, the values used in the subsequent simulations are summarized in Table 1.

The maximum number of generations (n_g) controls the algorithm's runtime and final population closeness to the Pareto front, where a larger number of generations allows for a more thorough search but increases computational cost. The individuals per generation (n_i) define the population size, affecting the genetic diversity of each population, convergence speed, and the computational cost of each population. Tournament participants determine the selection pressure during the tournament selection process. A selection probability of 90% indicates a high likelihood of selecting superior individuals, promoting faster convergence. A 5% mutation percentage ensures genetic diversity, adding random modifications to each offspring of a maximum of 5%, preventing premature convergence to local optima. A value too high for the mutation percentage can lead to convergence difficulties. The convergence delay (n_h) allows the algorithm to avoid early convergence measurement by avoiding hypervolume changes based on outlier populations with overly small changes in the hypervolume changes. We select a 10 for n_h as a trade-off between higher computational time and accuracy in the final converged output. The convergence tolerance (Tol) sets the precision for stopping criteria, ensuring the algorithm halts when improvements between the last n_h generations are marginal compared to the initial Pareto front area or hypervolume set according to the user. The design variable range for Z ($[Z_{\min}, Z_{\max}]$) and y ($[y_{\min}, y_{\max}]$) define the allowable limits for the crystal's half-length and height according to Fig. 5, ensuring feasible and practical solutions. The limits on these variables are set by the nominal half-length of the crystal of 28.5 and the space allocation for this detector crystals of 6 mm. The lower bound for the half-length of the crystal is set as a compromise so that the crystal can reduce its length and increase the light collection of impacts in $z = 0$, without unnecessarily extending the design space. The lower bound for the y nodal location is set to a small value higher than zero to avoid computational issues if part of the crystal has zero thickness during the random geometry generation by NSGA-II. The grid resolution parameter for the number of impacts as defined in Eq. (1) ($[n_x, n_z]$) dictates the balance of solution accuracy and computational efficiency, and is studied in the 1D solution. The values of 4 impacts through the half-x dimension and 15 impacts along the z direction showed, in the 1D analysis, to provide an error under 1% for the L_O and L_{SP} objectives for ten different evaluations, reducing computational time for a good result reliability compared to L_C.

Table 1. NSGA-II Parameters for Simulations

Parameter	Value
Maximum number of generations, n_g	100
Individuals per generation, n_i	100
Tournament participants	2
Selection probability	90%
Mutation percentage	5%
Convergence delay, n_h	10
Convergence tolerance, Tol	1%
$[Z_{\min}, Z_{\max}]$	[20 mm, 28.5 mm]
$[y_{\min}, y_{\max}]$	[0.1 mm, 3 mm]
$[n_x, n_z]$	[4,15]

Optimizations are performed for the same objectives studied in Section 3.A, including the mean and median values of the L_O, L_C, and L_{SP} photon counts. To study the convergence of these optimizations through the hypervolume we use its change concerning the hypervolume of the converged generation, for each generation of L_O and L_{SP}, which is plotted in Fig. 12(a). From this plot, we can further appreciate the difference in convergence rates of different objectives where $\overline{L_O}$ is the fastest and $\widetilde{L_{SP}}$ is the slowest in the 43 and 75 generations, respectively. The hypervolume value not only offers insights into the convergence rate but also serves as an indicator of the spatial distribution of the converged Pareto fronts. Specifically, the highest hypervolume of L_O is found to be 3.2×10^6, less than half of the smallest L_{SP} hypervolume of 7.8×10^6. This difference shows that the optimal designs within L_O are located within a significantly smaller region of the design space than the Pareto of L_{SP}. Due to the metaheuristic nature of NSGA-II, the hypervolume indicates when we are close to the Pareto front, which can be reached for multiple NSGA-II runs. However, we cannot ensure that we obtain the same individuals within the front between multiple runs, and the convergence rate can vary within the same orders of magnitude. These conclusions remain true for the objectives using the mean and median of each photon count distribution.

Figure 12 shows individuals close to Pareto fronts for the three different light collection measurements for the last NSGA-II generation run, and the volume value of the default initial configuration in Section 3.A as a dashed horizontal line. In each subplot of the Pareto front depicted in Fig. 12, there is a cross symbolizing the mean value of the distribution from the corresponding photon count measurement using the simplified geometry of the full resin width; see Fig. 9(a). This plot can provide further information comparing against the 513 mm^3 default bar design and the reference point, or nadir point, used for the hypervolume calculation, represented in the top right corner of each plot. The visually smoothest Pareto is obtained from the L_O optimization. However, the L_O optimizations converge to Pareto fronts at lower volumes compared to the other objectives, leading to subsequent lower photon counts. This observed effect is rectified in both L_C and L_{SP} objectives by incorporating the impacting particle's path length within the scintillator into the objective, either directly within L_{SP} or through the consideration of energy deposition in L_C.

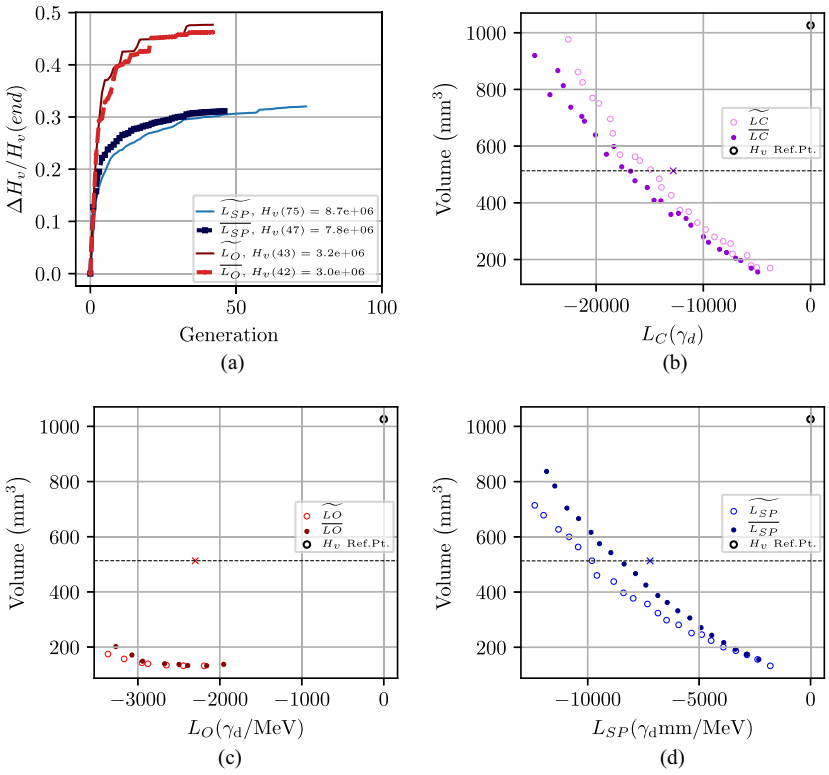

Fig. 12. Results for the bar configuration optimization with NSGA-II. (a) shows the hypervolume change with respect to the final calculated value with respect to the generation index and convergence satisfaction for the L_O and L_{SP} mean and median objectives. The results for a subset of the last NSGA-II generation is plotted in (b), (c), and (d) for the L_C, L_O, and L_{SP} mean and median objectives respectively. These plots include the original objective value for the bar configuration as a cross, its volume as a dashed horizontal line, and the nadir point as a circle in the top right of each figure.

From Fig. 12, it is evident that the rate of increase in the photon count measures slows as the values approach the maximum allowed volume. The individual with the maximum value is known and defined as the maximum thickness for all design variables, $\boldsymbol{\theta} == y_{\max}$, see Fig. 5. This maximum volume design results in a design featuring flat parallel surfaces, equivalent to the original design with a larger volume. Therefore, the optimal designs found in larger volumes have an active restriction on their thickness, limiting the design space. Expanding the ranges of θ for design variables that reside in the limits of the Pareto front may reveal better designs at these volumes.

A comparison of optimized results with respect to the default crystal bar volume allows us to discern the effects of the optimization between the P_{50} and mean objectives. When confronted with distributions that show tails at higher values, P_{50} tends to yield the most conservative results, focusing primarily on the lower values of the distribution. In contrast, for objectives such as L_O and L_{SP}, the mean results are more conservative, as P_{50} allows inclusion of lower-objective results while maintaining a higher value of P_{50}.

The resulting geometries for the same volume as the original bar, 513 mm^3, are plotted in Fig. 13. In the case of the objective L_O, the Pareto front does not reach the value of 513 mm^3 and we plot the results for the value of 200 mm^3, close to the highest volume found in the Pareto. These plots use the GMSH library to create the exact same mesh introduced in GEANT4 and are superposed to the default rectangular section. We can see from Fig. 13 that while the design is based on a spline, the number of nodes in the mesh affects the design, creating flat surfaces, which also affects the final design and its manufacturing. Furthermore, not all geometries have the same number of tetrahedral elements besides having the same number of nodes. This means that we can have geometries with far more complex meshes due to their shape, deteriorating the computational time.

Figure 13 not only gives information on the mesh of the models but also on the results from each different objective. The L_O objectives show a reduced thickness in the middle of the crystal bar that progressively increases toward its edges, ultimately covering a significant portion of the SiPM area at the crystal's end. Likewise, comparable trends are observed between the L_C and L_{ST} objectives for each of the used distribution metrics, median and mean values. This behavior is similar to the results obtained in the 1D study, where a lower energy deposition in the middle of the crystal is compensated by focusing of the photons into the SiPMs, and a higher sensitivity of the objective to impacts near the SiPMs. Concerning the median metric, both photon count objectives tend to decrease the thickness in the middle section of the crystal, as in the case L_O. This lower thickness results in lower energy deposition in the areas where the light output is the smallest due to a larger path length to the SiPM with a subsequent larger number of self-absorbed photons; see Fig. 7(b). In the case of objectives based on the mean of the distributions, both outcomes yield a wavy design that facilitates photons reaching SiPMs through successive reflections, featuring increased material concentrations in the middle of the crystal. This creates longer path lengths within the

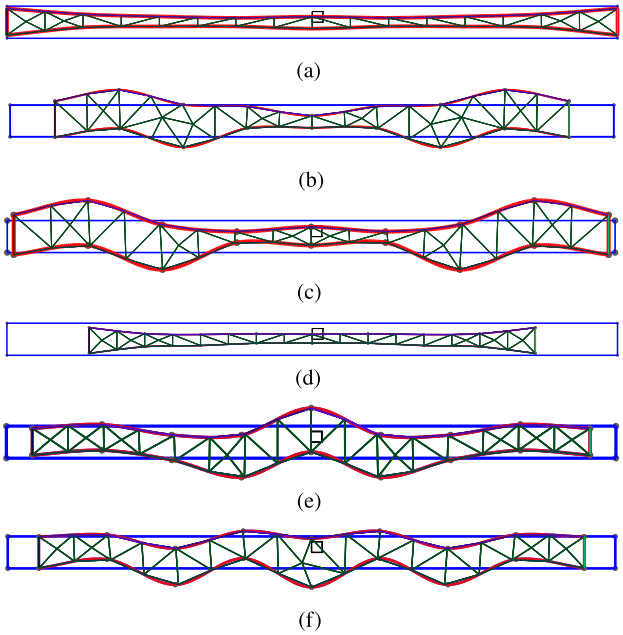

Fig. 13. Resulting geometries in GMSH for the last converged generation for multiple objectives, in red, superposed to the mesh used in GEANT4 and the original bar configuration in blue. The comparable geometries with the same volume provide the resulting objectives and their relative difference, Δ_r, to the corresponding values of the original simplified design in Fig. 9. (a) 200 mm^3, $\widetilde{L_O} = 3497$; (b) 513 mm^3, $\widetilde{L_C} = 14605$, $\Delta r = +14\%$; (c) 513 mm^3, $\widetilde{L_{SP}} = 10031$, $\Delta r = +38\%$; (d) 513 mm^3, $\overline{L_O} = 3062$; (e) 513 mm^3, $\overline{L_C} = 16780$, $\Delta r = +20\%$; (f) 513 mm^3, $\overline{L_{SP}} = 8535$, $\Delta r = +18\%$.

scintillator for ionizing particles and larger energy depositions, counteracting the lower light output previously observed in these regions for the default design. Furthermore, in these latest cases, the crystal is optimized to a smaller length and proportionally larger width, maintaining a constant sensitive area. This change reduces the overall photon path to the photodetector while increasing the losses in the SiPM interface—the SiPM size remains constant—to an optimum value. The gains of the optimized design can be obtained from the relative difference of the objectives to the original design,

$$\Delta_r = \frac{\Phi_i - \Phi_0}{\Phi_0}. \tag{18}$$

In Eq. (18), Φ_i is the photon count measure from the optimized design and Φ_0 the values from the original design, see Fig. 14. From this relative difference, we obtain the highest gains through the $\widetilde{L_{SP}}$ objective with a 38% increase. Other objectives provide more conservative gains between 15% and 20% for the same amount of volume.

While the Pareto fronts and resulting geometries offer insights into the algorithm's objectives, these solutions include errors stemming from the stochastic nature of GEANT4 ray-tracing simulations. Consequently, a thorough examination of each resulting individual is required to validate the accuracy of the photodetector photon counts with respect to the optimization outcomes. In Fig. 14, the results of each individual illustrated in Fig. 13 are presented using box plots for the various light measures employed in this study. Each box plot features the mean of the distribution marked with a red point, while the result obtained from the NSGA-II algorithm is denoted by a

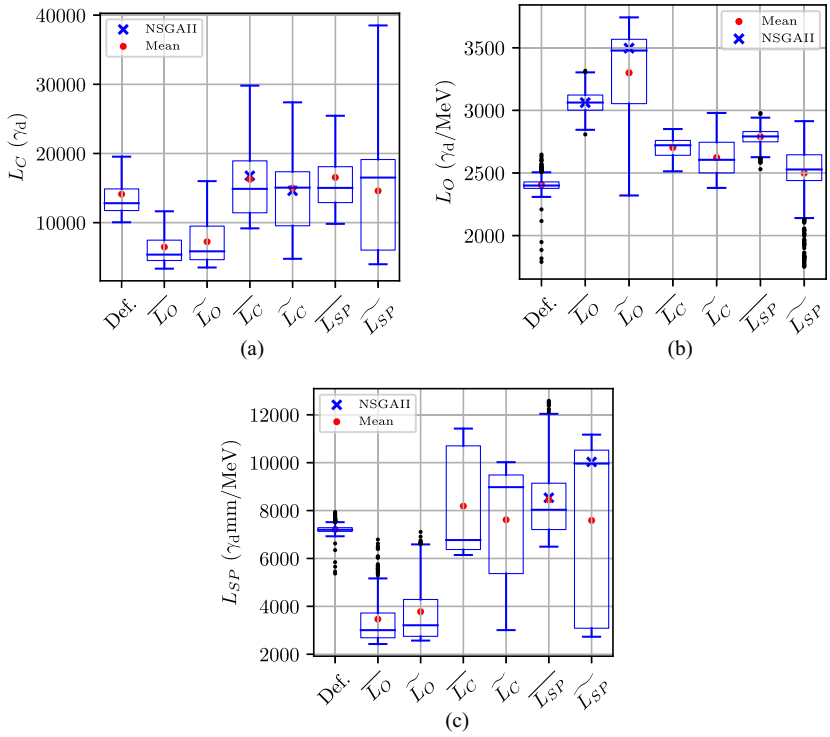

Fig. 14. Resulting light function distributions (L_O, L_C, and L_{ST}) as box plots against the default configuration (Def.) for three different objectives (L_O, L_C, and L_{ST}) and two distribution metrics (P_{50} and $\bar{x}$) for a volume of 513 mm^3 together with the corresponding scalar values obtained from the NSGA-II optimization as a blue cross.

dark blue star. For comparative analysis, the distributions for the initial default geometry (Def.) are included alongside the optimized crystal shapes. The NSGA-II results demonstrate a commendable alignment with the detailed light characteristics of each individual, as evidenced by the blue stars in Fig. 14. An exception to this pattern is observed in the optimization of L_C, where the error committed is approximately ±3% for each objective. In contrast, the error is considerably lower for L_O at 0.5% and for L_{SP} at 0.7%. The 1D model predicted these higher errors for the L_C objectives, see Fig. 11. These results suggest a higher reliability of the L_O and L_{SP} individuals that result at a comparable computational cost.

However, not all results from a different objective perform equally well in the other photon count metrics. The optimized results for L_O provide the highest L_O values compared to the other metrics but perform worse in total light collection. This is again due to the lack of impact of the path length of the ionizing particles within the crystal in this measure. We can also appreciate that the optimized results P_{50} displace the distribution toward larger light collections but do not introduce larger IQR values into the distributions. In the case of L_C, this more significant deviation is limited by the Landau distribution shape to larger values; however, for other objectives, this can introduce photon counts near to zero for certain impact locations. From these results, it becomes obvious that from the objectives studied, the $\overline{L_{ST}}$ provides a Pareto front with the largest gains in total light collection for any particle without reducing the minimum value of light collected and most accurate results with the same GEANT4 number of events. Using the results of the optimized results $\overline{L_{SP}}$ as a reference, we can further study the optimal result by comparing it with the original design depending on the position of the impact.

Figure 15 shows the L_{SP} objective for the original design in red and for the optimal design of the same volume in blue for half of the LYSO bar. This box plot still shows the expected parabolic profile in the default design; however, the values for the optimal design provide a much higher value for L_{ST} in each of the bumps due to the larger track-path length of the impacting particles within the scintillator. This can lead to more complex data processing with a larger variation of the photon count depending on the impact location.

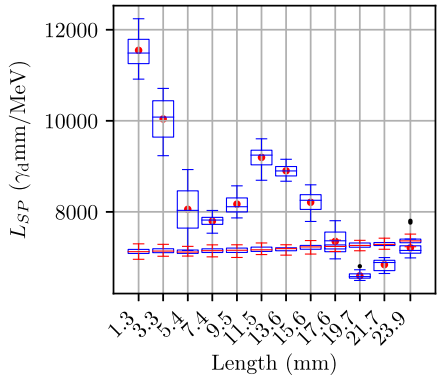

Fig. 15. L_{SP} distributions against the impact point along the z half-length of the optimal geometry obtained for the $\overline{L_{SP}}$ objective with 513 mm^3 and the default simplified geometry.

2. Tile Configuration

The previous optimization, based on Fig. 5, uses an extrusion of a 2D profile to simplify crystal manufacturing. However, this can lead to lower light collections compared to a full surface optimization. Using the configuration with SiPMs at the bottom of the LYSO crystals or tile configuration, and the parameterization described in Fig. 6, we can perform a complete surface shape optimization.

To perform this optimization, we focus on the $\overline{L_{SP}}$ objective given the results in Fig. 14. Furthermore, this optimization includes the position of the SiPM in the bottom $y == 0$ plane as a variable defined in Eq. (11). In this case, since we are only displacing the location of the y nodes from the top surface, rather than the bottom and top as in the bar configuration, we modify the variable limits to

$$[y_{\min}, y_{\max}] = [0.85\ \text{mm}, 6\ \text{mm}]. \tag{19}$$

This maintains the maximum height of the scintillator below 6 mm using a single control point for the top surface following Fig. 6. The only other change from the parameters in Table 1 is the pattern of impact points set to

$$[n_x, n_z] = [6, 6], \tag{20}$$

using a lower number of impacts compared to the previous simulations. This is helpful in reducing the computational time along the optimization process, as a larger computational complexity is expected of this problem, which has more design freedom than previous ones. This extra computational complexity or computation time arises from the larger number of elements created to define the geometry that needs to be evaluated in the photon paths.

The results of this optimization provide a new Pareto front plotted in Fig. 16. This figure shows a Pareto front with higher $\overline{L_{SP}}$ for intermediate volume objective values than the previous case, highlighting the influence of initial parameterization and design freedom on the results.

In particular, we find that for a volume of 490 mm, we obtain a relative gain with the default bar configuration of up to 47%, $\overline{L_{SP}} = 10584$, compared to the previous value of 18%. The resulting geometry for this particular individual is represented in

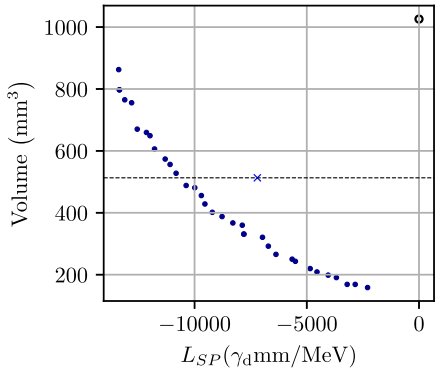

Fig. 16. Pareto front for the tile configuration, see Fig. 6. The plot includes the volume objective and the negative $\overline{L_{SP}}$ in the y and x axis, respectively. The plot also includes the reference point H_v in black and the default configuration $\overline{L_{SP}}$ as a blue cross.

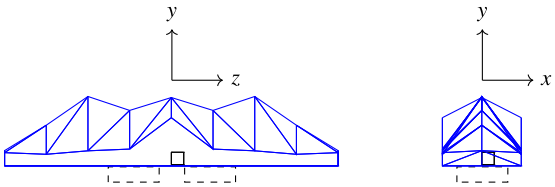

Fig. 17. (a) Front and (b) lateral view of the resulting geometries from GMSH for the last converged generation for the tile, see Fig. 6. The results are obtained from the Pareto front at a volume of 490 mm. The individual has an objective value of $\overline{L_{SP}} = -10588$ with a relative gain of 47%.

Fig. 17 with two lateral views corresponding to the projections of the plane x-y and y-z.

This result has a Z_S value of 25%, which locates the center of the SiPM below the first node from the center of the crystal in z. Furthermore, the optimization creates an inclined top surface with lower thickness towards the edges. This has two effects: firstly, it redirects photons toward the central region of the crystal, precisely where the SiPMs are positioned; secondly, it induces a lower-energy deposition at a greater distance from the SiPMs.

This new configuration, while attractive because of a larger light collection, has some disadvantages. In particular, the manufacturing of the optical surfaces becomes more complex and we have a larger dependence of the light collection over the y impact locations. Furthermore, the discretization of the surface does not ensure a smooth contour as we would obtain with a spline definition.

We still need to verify the results of the NSGA-II algorithm, as the lower number of impacts can impose a greater error on the objective values L_{SP}. Running a Monte Carlo study on the optimal configuration shown in Fig. 17, we can obtain an accurate prediction of its L_O distributions at the cost of a larger computational complexity, which is not feasible for optimization purposes. Furthermore, we can also try to discern the design criterion that the algorithm applies to the design of these crystals by investigating the dependence of L_{SP} on the impact locations. This verification shows a resulting mean of 8950, with a relative gain of 24% rather than 47% for the optimal design. This means that we have an overestimation of the objective of the photon count in the Pareto front of 18% with respect to the default bar configuration measure. To better understand the source of these differences and the inner workings of the algorithm, we need to understand the effect of the location of the particle impacts on the geometry.

Figure 18 shows the dependence of L_{SP} with the impact locations along z and x based on the verification Monte Carlo analysis. The distributions in Fig. 18(a) show the variation of the L_{SP} depending on the z axis impact location while Fig. 18(b) shows this effect along the x axis, including each distribution's percentiles, means, and outliers. From these figures, we deduce that the algorithm maximizes the light collection from the central location of the crystal in x and z, disregarding the effects of the edges along x and z. From these plots, we can also see that the use of more than one row of control points along x leads to a clear dependence on the output mean with regard to this axis. This dependence seems to correlate with the overall thickness change in each region linearly. The disregard of the edge locations can be related to the smaller number of impact points, with larger gaps in these regions.

These results suggest that a low number of impacts can provide improved scintillator geometries at a lower computational cost. However, the objective functions for the scintillator optimizer are sensitive to the impact locations studied and should be selected for each particular case so as not to detriment the optimization procedure and limit the objective value variability over multiple evaluations.

4. CONCLUSIONS

In this paper, we have introduced a novel approach that involves design criteria and modeling techniques to increase the light collection of scintillation crystal-based photodetectors with GEANT4. Moreover, we conducted a comprehensive comparison of different optimization objectives capable of modifying the resulting light collection distributions while keeping constant the material-associated costs. Through our research, we have found that neither the light collection nor the light output are adequate indicators of the problem. Instead, we propose a new objective function based on the light collection per pseudo-stopping power, L_{SP}, which yields improved Pareto fronts, objective distributions, and convergence for this problem. These studies have been performed through a

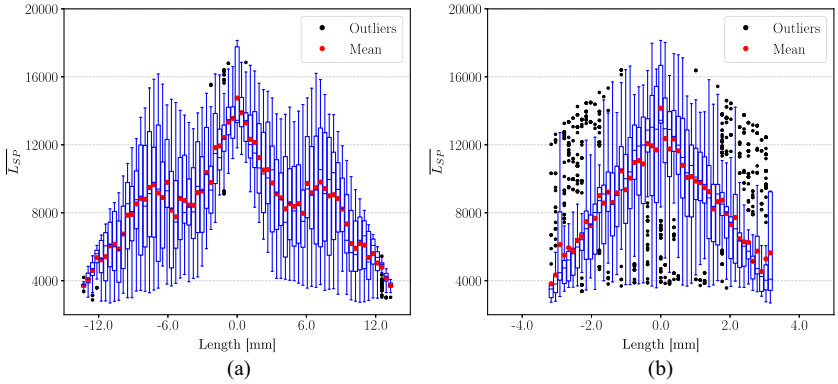

Fig. 18. $\overline{L_{SP}}$ for an optimized LYSO:Ce tile configuration with respect to the impact location using a random impact pattern. (a) shows the distribution effect with respect to the z impact location while (b) shows the dependence of the x impact location.

simplified 1D model to isolate the influence of the reflective surfaces and energy deposition from the material volume and study the problem fitness. The results of this 1D model have then been extrapolated to a multidimensional optimization and compared, obtaining design criteria for the LYSO:Ce crystals. Although this model is capable of predicting the fitness of the problem and expected errors due to the stochastic nature of the problem, the problem could be further studied through landscape analysis at a possible higher computational cost and lower pre-processing required to simplify the problem in question [38].

Compared to the previous literature on the optimization of scintillator geometries, we provide a shape optimization capable of higher flexibility and generalizability of the design methodology rather than the commonly used parametric optimization with predispositions made by the designers [18,21]. The multiple-objective study looks into the overall light collection using a multi-objective optimizer. The focus on the light collection can be seen to be related to the timing of the detector [39]. However, using the light collection as a single objective can lead to larger widths for the optimized distributions, which is the focus of previous optimizations [19,21]. The formulation with NSGA-II allows for the introduction of multiple objectives that could ensure the selection of shapes with the highest light collection, highest time precision, and smallest distribution width with the addition of the extra objectives and a higher computational cost. Some proposed objectives to reduce the width of these distributions are the interquartile range (IQR) for non-symmetrical distributions or the minimum values within the distribution. We also notice that the use of normalization techniques could improve the behavior of some of the objectives in multi-objective optimization, and techniques to deal with the stochastic noise could reduce the objective variability between different runs, such as dynamic sampling rates, during the optimization.

Furthermore, our results emphasize the critical role of the SiPM or photodetector model and its location in achieving overall detector efficiency; notice how the ends of the crystals always adapt to the photodetector shape. The impact of SiPMs on the collection area is appropriately recognized, and we underscore the importance of considering the SiPM power needs and its changes with its area under a joint LYSO-SiPM optimization. Additionally, our optimal results reveal that a larger crystal area in contact with the SiPM module may lead to higher losses to the environment. Nevertheless, in the bar configuration, this decrease in performance from a larger contact area can be counteracted by a lower length of the overall crystal.

In addition to the photodetector mode, the material models have an impact on the results. Our material models are derived from measured prototypes, which serve as a valuable guide for future designs. However, there is limited information available on scintillating materials, which should be considered when interpreting the model output. However, because the LYSO:Ce crystals have a non-negligible cost, experimental tests are limited. In the case of plastic scintillators, which present lower light yields and refractive indexes, the optimization results are speculated to provide lower gains based on the reflective surfaces under a direct air–scintillator interface. This could be mitigated through directly deposited reflective coatings, increasing the objective sensitivity to these surfaces. The use of non-polished surfaces also shows promise in increasing light collection in scintillator-based detectors [14]. According to our model, we can reduce material costs without losing light collection efficiency. Nevertheless, the resulting shapes might require the use of free-form optics. This manufacturing technology is relatively recent, and there is no current good way to estimate the cost of these intricate shapes derived by optimization. As this complexity increases, careful evaluation of the associated manufacturing cost becomes essential. This paper deals with the optimization of a BTL-based design, which limits the variability of surface roughness of the crystals and their coatings. However, the use of localized surface treatments could be introduced as a further design variable, alleviating the manufacturing constraints and potentially modifying the light collection and timing. For experimental testing of the optimal results, plastic scintillators also have an advantage as they can be easily machined and are less expensive.

Despite the potential of our automated design procedure to enhance performance and reduce costs, further investigation and access to cluster computing tools are currently necessary due to the computational demands of genetic algorithms and ray-tracing software, with its associated costs. Nevertheless, our research highlights the potential for numerical optimization in particle detectors, extending its applicability beyond scintillation material modeling to the optical interfaces of the assembly. To further tackle the computational challenges arising from the lack of sensitivities in Monte Carlo-based problems, we suggest exploring methods such as finite element method (FEM) or finite difference time domain (FDTD) to incorporate scintillation models and improve computational efficiency.

As the field of numerical optimization in particle detectors continues to evolve, we anticipate numerous opportunities for improvement and new discoveries, not only in scintillation geometries but also in the optical interfaces of the assembly. Additionally, the recent application of 3D printing technologies to the manufacturing of scintillators opens new avenues for utilizing this optimization approach. Furthermore, the insights obtained from our study can be extrapolated to different detector geometries, such as fiber-based ones, as well as other detector types where shape optimization can increase efficiency. We strongly encourage further exploration in these areas to broaden the scope of this optimization technology.

In conclusion, our work presents valuable insights and guidelines for designing efficient and cost-effective scintillation-crystal-based photodetectors, serving as a foundation for future research and advancements in this domain. By considering the proposed optimization objectives and modeling techniques, researchers can make informed decisions to enhance the performance of particle detectors and drive innovation in the field.

APPENDIX A: MATERIAL DATA

In this appendix, we provide the material data used in the model within GEANT4 to facilitate the reproduction of the results in this paper.

Table 2. Material Compositions Used in the GEANT4 BTL Module Model

	Composition	Density (kg/m^3)
LYSO:Ce	$(Lu_{2(1-x)}Y_{2x}SiO_5)_yCe_{1-y}$	7125
Epoxy resin	$H_{32}N_2C_{15}O_4$	1160
RTV3145	$H_5Si_3O_5C_5$	1270
Silicon	Si	2400
SiO_2	SiO_2	2201
FR_4	$(SiO_2)_{0.528}Epoxy_{(0.472)}$	1451

1. MATERIAL COMPOSITION

The material composition and density are required for the energy deposition calculations. The properties of all the materials involved are summarized in Table 2.

The LYSO:Ce composition, follows a density value dependent upon the Y content that was fitted in [32] to the linear equation:

$$\rho_L = 7390 - 3020x. \tag{A1}$$

In Eq. (A1), x represents the Y percentage and its relation to the LYSO:Ce density, ρ_L, in kg/m^3. Fixing the density of the crystal to the most common measured value in [32], 7125 kg/m^3, we obtain a percentage of the mass of Ce given by $x = 0.0877$ in the LYSO:Ce composition. The percentage of Ce is fixed by a given value of $y = 0.981$, equivalent to 0.19% of Ce.

2. OPTICAL PROPERTIES

In the context of the light propagation within the detector assembly, the material properties to include in the model are the refractive index, absorption coefficient, and scattering coefficient of the different materials involved.

A. Refraction Index

An accurate refractive index is required for a correct material boundary simulation for each photon trace. Furthermore, the different wavelengths and the dependence of the refractive index on their energy can lead to different outcomes.

The refractive index of the LYSO, optical glue coupling, and epoxy resin is summarized in Fig. 19. These materials are the most influential in the path of the photons as they will need to go through their interfaces before reaching the photodetectors.

For the rest of the materials, we assume a constant refractive index with respect to the involved photon wavelengths. These properties are summarized in Table 3.

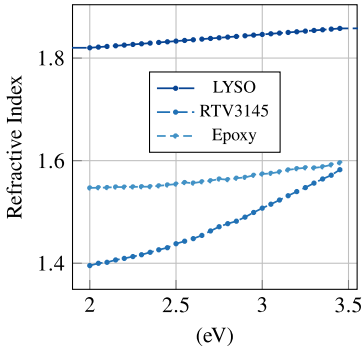

Fig. 19. LYSO [32], optical glue (RTV3145), and protective epoxy resin [40] refractive index depending on the photon wavelength or energy.

Table 3. Material Compositions Used in the GEANT4 BTL Module Model

	Refractive Index	References
Air	1	[22]
Si	4	[41]
SiO_2	1.4585	[41]
FR_4	1.4585	[41]

B. Self-Absorption Lengths

In the context of optical materials, wherein photons traverse the majority of their trajectory enroute to the Silicon Photomultiplier (SiPM), the potential for re-absorption is a noteworthy consideration. To address this concern, we establish the self-absorption length of both the adhesive substance and the LYSO with respect to photon energy, as illustrated in Fig. 20. These data serve as input for the GEANT4 simulation framework, enabling the determination of a threshold path length for the termination of generated photons.

The rest of the components do not include self-absorption for simplification purposes.

C. Scattering Lengths

The scattering length, as illustrated in Fig. 21, is delineated across the x axis, representing the photon energies. Notably, while the scattering length for LYSO is meticulously characterized and highlighted in the figure, it is intentionally neglected for all other materials.

D. Enhanced-Specular-Reflector (ESR)

In order to prevent the loss of photons in the surrounding environment and reduce the occurrence of false positives, it is common practice to coat or cover scintillators with a reflective layer. In our model, we employ an enhanced specular reflector (ESR) layer covering the LYSO, maximizing the air–LYSO contact area to capitalize on the substantial refractive index

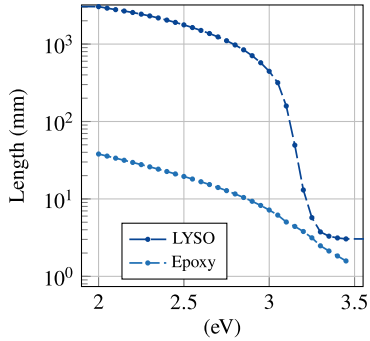

Fig. 20. Self-absorption and scattering lengths for LYSO [42] and protective epoxy resin depending on the photon wavelength or energy [40].

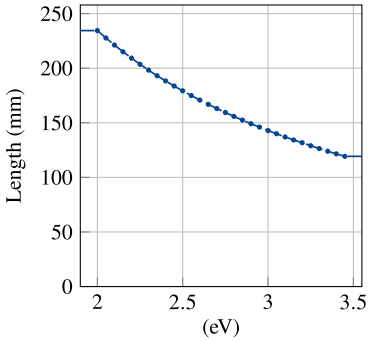

Fig. 21. Scattering length for LYSO [42].

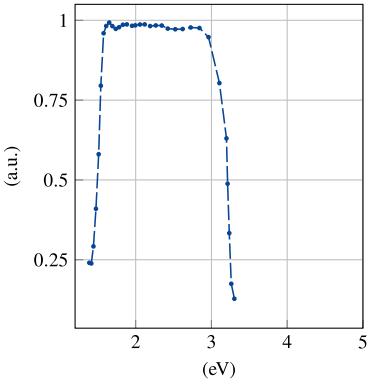

Fig. 22. ESR reflectivity as a function of the incident photon wavelength for multiple incident angles [44].

difference between these materials, which enhances the probability of photon reflection back into LYSO:Ce [34]. To achieve this, we use the *polishedbackpainted* model of GEANT4, which accounts for a thin layer of air without the need for an explicit geometric definition.

The ESR is assumed to be a perfect specular reflector [43], which does not include backscatter, Lambertian reflection, or specular spikes, as supported by the measurements presented in [44] and [45]. The reflectivity of the ESR, which represents the likelihood of an impacting photon to be reflected rather than absorbed, is illustrated in Fig. 22.

From the data available for multiple impact angles, we use the most limiting at 60 deg. This reflectivity still provides reflectivity values higher than 0.98 for the wavelengths measured by the LYSO scintillator.

3. LYSO:Ce SCINTILLATION

The LYSO:Ce crystals or scintillator for the particle detector need to be characterized in terms of light yield (L_Y)—the number of photons created within the scintillator per unit of energy deposited. To ensure accuracy in the model, we rely on the crystal properties measured in [32,33]. In contrast, other research works, such as [42,46], propose their own models, which further validate the material properties chosen.

Figure 23 provides the intensity of photon creation for each possible wavelength, with a nominal L_Y of 40000 γ/MeV.

Furthermore, to simplify the model, we select a r_s of zero with no statistical variance of L_Y. Finally, the time characteristics

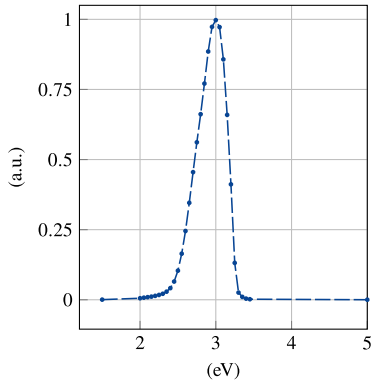

Fig. 23. LYSO emission spectra [32,33].

Table 4. Characteristics of the LYSO Scintillation Process Used in GEANT4 [33]

r_s	τ_r (ns)	τ_d (μs)	L_Y (γ/MeV)
0	60	39.1	40000

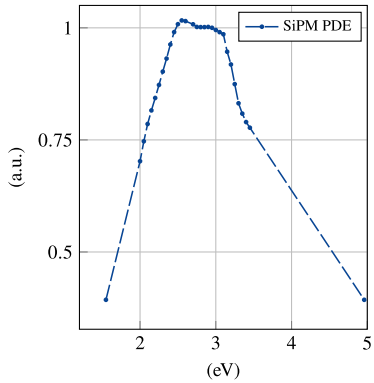

Fig. 24. 420 nm S13360-1325CS normalized PDE_λ.

are given as a single rise and decay times of 60 ns and 39.1 μs respectively. These values are summarized in Table 4. These timing quantities for the LYSO scintillation measured in [33] by the light detected from the crystals encompass the characteristic delay from the Ce_3^+ absorption and re-emission.

4. SILICON PHOTOMULTIPLIER (SiPM) DETECTION

The SiPMs have a certain photon detection efficiency (PDE), which determines if a photon impact is detected. This PDE depends upon the photon energy and the overvoltage applied. For this purpose, we use the PDE characteristics given by Hamamatsu of the S13360-1325CS SiPM adimensionalized with respect to its 420 nm value, Fig. 24.

The measured dependence of the rest of the spectrum is considered linear with respect to the 420 nm peak and is represented by Eq. (6).

Funding. U.S. Department of Energy.

Acknowledgment. The authors also express appreciation to the MTD collaboration members for their invaluable contributions.

Disclosures. The authors declare no conflicts of interest.

Data availability. The code used to obtain the results in this paper can be found in the SO-CRYSTAL repository [47]. Data underlying the results presented in this paper are not publicly available at this time but may be obtained from the authors upon reasonable request.

REFERENCES

1. Z. Wang, C. Dujardin, M. S. Freeman, *et al.*, "Needs, trends, and advances in scintillators for radiographic imaging and tomography," IEEE Trans. Nucl. Sci. **70**, 1244–1280 (2023).
2. C. Dujardin, E. Auffray, E. Bourret-Courchesne, *et al.*, "Needs, trends, and advances in inorganic scintillators," IEEE Trans. Nucl. Sci. **65**, 1977–1997 (2018).
3. J. Liu, X. Zhao, Y. Xu, *et al.*, "All-inorganic glass scintillators: scintillation mechanism, materials, and applications," Laser Photon. Rev. **17**, 2300006 (2023).
4. P. Lecoq, "Development of new scintillators for medical applications," Nucl. Instrum. Methods Phys. Res. A **809**, 130–139 (2016).
5. F.-M. Lu and Z. Yuan, "PET/SPECT molecular imaging in clinical neuroscience: recent advances in the investigation of CNS diseases," Quant. Imaging Med. Surg. **5**, 433–447 (2015).
6. Y. Kharzheev, "Scintillation detectors in modern high energy physics experiments and prospect of their use in future experiments," J. Lasers Opt. Photon. **4**, 1000148 (2017).
7. J. Glodo, Y. Wang, R. Shawgo, *et al.*, "New developments in scintillators for security applications," Phys. Proc. **90**, 285–290 (2017).
8. C. Kim, W. Lee, A. Melis, *et al.*, "A review of inorganic scintillation crystals for extreme environments," Crystals **11**, 669 (2021).
9. R.-Y. Zhu, "Summary talk in CEPC calorimetry workshop at IHEP, Beijing," March 14, 2019, https://www.its.caltech.edu/~rzhu/talks/ryz_190314_CEPC_summary.pdf.
10. A. Pla-Dalmau, A. D. Bross, and K. L. Mellott, "Low-cost extruded plastic scintillator," Nucl. Instrum. Methods Phys. Res. A **466**, 482–491 (2001).
11. R.-Y. Zhu, "Ultrafast and radiation hard inorganic scintillators for future HEP experiments," J. Phys. Conf. Ser. **1162**, 012022 (2019).
12. Y. N. Kharzheev, "Radiation hardness of scintillation detectors based on organic plastic scintillators and optical fibers," Phys. Part. Nucl. **50**, 42–76 (2019).
13. S. Cherny, "Problems in the use of plastic scintillators in intense radiation fields," Radiat. Phys. Chem. **41**, 181–184 (1993).
14. S. Xie, X. Zhang, Y. Zhang, *et al.*, "Evaluation of various scintillator materials in radiation detector design for positron emission tomography (PET)," Crystals **10**, 869 (2020).
15. I. V. Khodyuk, S. A. Messina, T. J. Hayden, *et al.*, "Optimization of scintillation performance via a combinatorial multi-element co-doping strategy: application to NaI:Tl," J. Appl. Phys. **118**, 084901 (2015).
16. E. Berg, E. Roncali, and S. R. Cherry, "Optimizing light transport in scintillation crystals for time-of-flight PET: an experimental and optical Monte Carlo simulation study," Biomed. Opt. Express **6**, 2220–2230 (2015).
17. F. A. Danevich, R. V. Kobychev, V. V. Kobychev, *et al.*, "Optimization of light collection from crystal scintillators for cryogenic experiments," Nucl. Instrum. Methods Phys. Res., Sect. A **744**, 41–47 (2014).
18. S. Min, Y. Kim, K. H. Ko, *et al.*, "Optimization of plastic scintillator for detection of gamma-rays: simulation and experimental study," Chemosensors **9**, 239 (2021).
19. Z. Li, Z. Pan, and G. Hu, "Optimization for energy response characteristics of plastic scintillators based on genetic algorithm," AIP Adv. **12**, 115111 (2022).
20. J. A. Kulesza, T. R. Adams, J. C. Armstrong, *et al.*, "MCNP code version 6.3.0 theory and user manual," Technical Report LA-UR-22-30006, Rev. 1 (2022).
21. B. Zhao, M. Dong, M. Zhou, *et al.*, "Optimization of the scintillator units for the CEPC scintillator - tungsten ECAL," Radiat. Detect. Technol. Methods **4**, 39–45 (2020).
22. S. Agostinelli, J. Allison, K. Amako, *et al.*, "GEANT4-a simulation toolkit," Nucl. Instrum. Methods Phys. Res. A **506**, 250–303 (2003).
23. L. M. Rios and N. V. Sahinidis, "Derivative-free optimization: a review of algorithms and comparison of software implementations," J. Global Optim. **56**, 1247–1293 (2013).
24. S. Kumar, Z. Tong, and X. Jiang, "Advances in the design and manufacturing of novel freeform optics," Int. J. Extrem. Manuf. **4**, 032004 (2022).
25. Collaboration CMS, "A MIP timing detector for the CMS phase-2 upgrade," Technical Report CERN-LHCC-2019-003 (CERN, 2019), https://cds.cern.ch/record/2667167.
26. K. Deb, A. Pratap, S. Agarwal, *et al.*, "A fast and elitist multiobjective genetic algorithm: NSGA-II," IEEE Trans. Evol. Comput. **6**, 182–197 (2002).
27. Geant4 Collaboration, *Physics Reference Manual. GEANT4: A Simulation Toolkit Manual*, Vol. **1** (2019).
28. C. Geuzaine and J.-F. Remacle, "GMSH: a three-dimensional finite element mesh generator with built-in pre- and post-processing facilities," Int. J. Numer. Meth. Eng. **79**, 1309–1331 (2009).
29. C. M. Poole, I. Cornelius, J. V. Trapp, *et al.*, "Fast tessellated solid navigation in GEANT4," IEEE Trans. Nucl. Sci. **59**, 1695–1701 (2012).
30. E. Sysoeva, V. Tarasov, and O. Zelenskaya, "Comparison of the methods for determination of scintillation light yield," Nucl. Instrum. Methods Phys. Res., Sect. A **486**, 67–73 (2002).
31. S. E. Derenzo, W. S. Choong, and W. W. Moses, "Fundamental limits of scintillation detector timing precision," Phys. Med. Biol. **59**, 3261–3286 (2014).
32. F. M. Addesa, P. Barria, R. Bianco, *et al.*, "Comparative characterization study of LYSO:Ce crystals for timing applications," J. Instrum. **17**, P08028 (2022).
33. M. Campana and R. Paramatti, "Study of light output and characterization of LYSO crystals for the new timing detector of the CMS experiment," Ph.D. thesis (Sapienza – University of Rome, 2019).
34. F. Loignon-Houle, C. M. Pepin, S. A. Charlebois, *et al.*, "Reflectivity quenching of ESR multilayer polymer film reflector in optically bonded scintillator arrays," Nucl. Instrum. Methods Phys. Res. A **851**, 62–67 (2017).
35. M. Li and X. Yao, "Quality evaluation of solution sets in multiobjective optimisation: a survey," ACM Comput. Surv. **52**, 26 (2019).
36. A. Auger, J. Bader, D. Brockhoff, *et al.*, "Hypervolume-based multiobjective optimization: Theoretical foundations and practical implications," Theor. Comput. Sci. **425**, 75–103 (2012).
37. A. P. Guerreiro, C. M. Fonseca, and L. Paquete, "The hypervolume indicator: computational problems and algorithms," ACM Comput. Surv. **54**, 119 (2021).
38. K. M. Malan, "A survey of advances in landscape analysis for optimisation," Algorithms **14**, 40 (2021).
39. E. Auffray, B. Frisch, F. Geraci, *et al.*, "A comprehensive and systematic study of coincidence time resolution and light yield using scintillators of different size, wrapping and doping," in *IEEE Nuclear Science Symposium Conference Record* (2011), pp. 64–71.
40. M. Montecchi and Q. Ingram, "Study of some optical glues for the compact Muon Solenoid at the Large Hadron Collider of CERN," Nucl. Instrum. Methods Phys. Res., Sect. A **465**, 329–345 (2001).
41. https://refractiveindex.info/.
42. D. J. Van Der Laan, D. R. Schaart, M. C. Maas, *et al.*, "Optical simulation of monolithic scintillator detectors using GATE/GEANT4," Phys. Med. Biol. **55**, 1659–1675 (2010).
43. M. Janecek and W. W. Moses, "Optical reflectance measurements for commonly used reflectors," (2009), https://escholarship.org/uc/item/82r9k9rn.
44. F. Padera and C. Lynch, "Measurement of enhanced specular reflector (ESR) films using a lambda 1050+ UV/VIS/NIR spectrometer and URA accessory," (2015), https://www.perkinelmer.com/.
45. M. Janecek, "Reflectivity spectra for commonly used reflectors," (2012), https://escholarship.org/uc/item/75v883cf.
46. J. M. C. Brown, S. E. Brunner, and D. R. Schaart, "A high count-rate and depth-of- interaction resolving single-layered one-side readout pixelated scintillator crystal array for PET applications," IEEE Trans. Radiat. Plasma Med. Sci. **4**, 361–370 (2019).
47. G. R. Gutiérrez, "SO-CRYSTAL," Zenodo (2024), https://zenodo.org/doi/10.5281/zenodo.11127324.